

# Experimental Characterization of a Large-Range Parallel Kinematic XYZ Flexure Mechanism

Shorya Awtar<sup>1</sup>

Precision Systems Design Laboratory, Mechanical Engineering,  
University of Michigan,  
Ann Arbor, MI 48109  
e-mail: awtar@umich.edu

Jason Quint

Precision Systems Design Laboratory, Mechanical Engineering,  
University of Michigan,  
Ann Arbor, MI 48109  
e-mail: jasonqu@umich.edu

John Ustick

Precision Systems Design Laboratory, Mechanical Engineering,  
University of Michigan,  
Ann Arbor, MI 48109  
e-mail: ustickj@gmail.com

Previously, we reported the conceptual design of a novel parallel-kinematic flexure mechanism that provides large and decoupled motions in the X, Y, and Z directions, along with good actuator isolation, and small parasitic error motions (Awtar, S., Ustick, J., and Sen, S., 2012, "An XYZ Parallel-Kinematic Flexure Mechanism With Geometrically Decoupled Degrees of Freedom," *ASME J. Mech. Rob.*, 5(1), p. 015001). This paper presents the detailed design and fabrication of a high-precision experimental setup to characterize and validate the motion attributes of this proposed flexure design via comprehensive measurements. The unique aspects of this experimental setup include a novel modular construction and exact-constraint assembly of the flexure mechanism from 12 identical parallelogram flexure modules. The flexure mechanism along with the sensing and actuation setup in the experiment is designed to enable large range (10 mm) in each direction. Experimental measurements and finite-elements analysis demonstrate <3% variation in motion direction stiffness, 20.4% lost motion, <11.6% cross-axis error, <3.3% actuator isolation, and <9.5 mrad motion stage rotation over the entire 10 mm × 10 mm × 10 mm range of motion. [DOI: 10.1115/1.4048259]

**Keywords:** compliant mechanism, mechanism design, parallel kinematic

## 1 Introduction and Background

In a previous paper [1], we reported the design and analysis of a novel parallel-kinematic flexure mechanism, shown in Fig. 1, that provides highly decoupled motions along the three translational directions (X, Y, and Z) and high stiffness along the three rotational directions ( $\theta_x$ ,  $\theta_y$ , and  $\theta_z$ ). The X-, Y-, and Z directions thus represent degrees-of-freedom (DoF), and the  $\theta_x$ ,  $\theta_y$ , and  $\theta_z$  represent degrees of constraint (DoC). In that paper, we analyzed the

design via nonlinear finite-elements analysis (FEA) and validated the predicted large range and decoupled motion capabilities by fabricating and physically inspecting a proof-of-concept prototype shown in Fig. 1. However, given the simplistic nature of this prototype and lack of any sensors, any experimental measurement of the various motion attributes was not possible. In the current paper, we present the detailed design of a new experimental setup, shown in Fig. 2, with the objective of performing and reporting accurate, repeatable, and comprehensive measurements of the motion attributes of the proposed flexure mechanism.

This flexure mechanism comprises eight rigid stages at the corners inter-connected by parallelogram flexure modules (PFMs). Each PFM serves as a single translational DoF constraint element. The PFMs serve to transmit motion from the actuation stages (labeled X, Y, and Z in Fig. 1) through the intermediate stages (XY, XZ, YZ) and on to the motion stage (XYZ). The green PFMs (G1 through G4) deform primarily in the X direction and remain stiff in all other directions; the red PFMs (R1 through R4) deform primarily in the Y direction and remain stiff in all other directions; and, the blue PFMs (B1 through B4) deform primarily in the Z direction and exhibit high stiffness in all other directions. A more detailed explanation of the synthesis and operation of this flexure mechanism design may be found in Ref. [1].

This arrangement of rigid stages and PFM constraint elements provides the following motion attributes, which are generally desirable in multi-axis parallel-kinematic flexure designs:

- (1) *Large motion range.* In order to satisfy this requirement, the flexure bearing must have low *actuation stiffness* along the DoF (or primary motion directions). Additionally, it should provide *geometric decoupling* between these DoF, i.e., actuation stiffness along one DoF direction should remain largely invariant to actuation along other DoF directions.
- (2) *Small cross-axis error motion.* Actuation along one DoF should not induce motions along the other DoFs at the motion stage.
- (3) *Small parasitic rotations.* Actuation along any of the DoF should not induce motions along the DoCs at the motion stage.
- (4) *Good actuator isolation.* The point of actuation for a given DoF should be well guided along that DoF and should not be influenced by the actuation in other DoF directions.
- (5) *Small lost motion.* The motion difference between the point of actuation and the motion stage along a given DoF should be minimal. Correspondingly, the *transmission stiffness* between the point of actuation and the motion stage should be high.
- (6) *Overall compact design.* It is desirable to achieve these attributes in a compact a size design since most applications will have some space constraints.

Several multi-axis parallel-kinematic flexure mechanisms have been reported in the literature. Appendix presents a table that

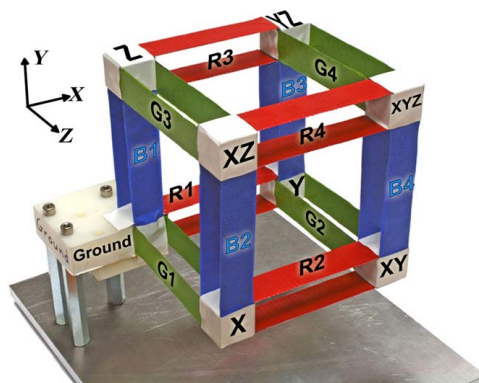


Fig. 1 Proof-of-concept prototype: XYZ flexure mechanism

<sup>1</sup>Corresponding author.

Contributed by the Mechanisms and Robotics Committee of ASME for publication in the *JOURNAL OF MECHANISMS AND ROBOTICS*. Manuscript received February 16, 2020; final manuscript received July 30, 2020; published online October 7, 2020. Assoc. Editor: Stephen Canfield.

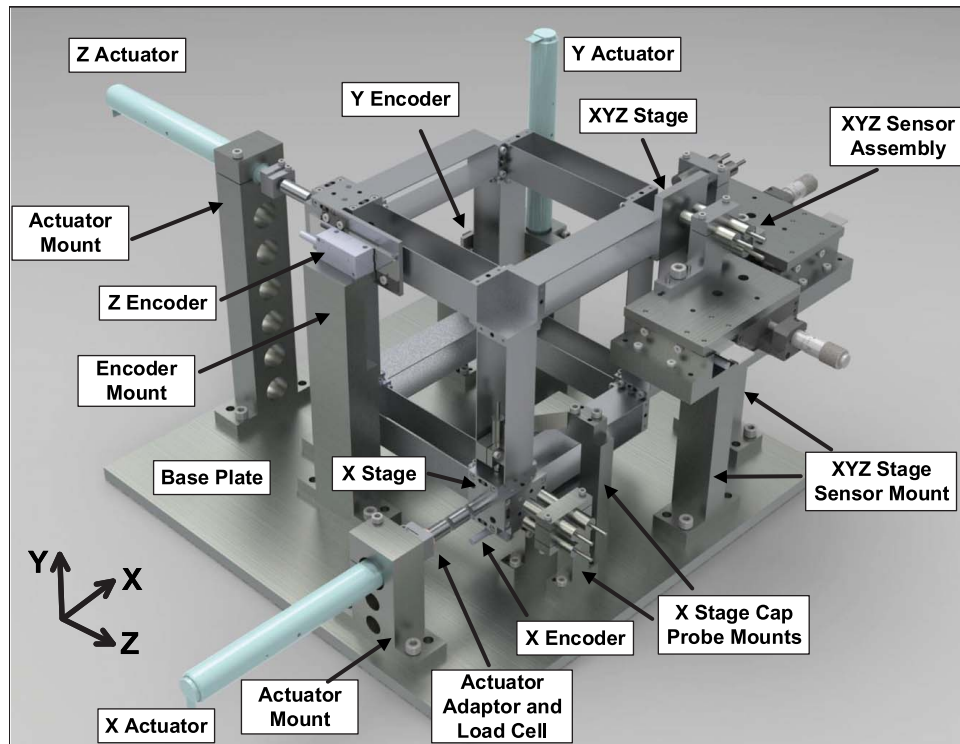


Fig. 2 Experimental setup to test the motion attributes of the proposed XYZ flexure mechanism

reviews 13 different designs with respect to the aforementioned attributes. The majority of these designs offer limited motion range due to inadequate geometric decoupling and actuation isolation between the multiple DoF. References [2,3] provide a geometrically decoupled XYZ flexure mechanism, using a constraint-based approach, very similar to the original design proposed in Ref. [1] but report a relatively smaller motion range ( $\sim 0.6$  mm) for the overall mechanism size ( $[100 \text{ mm}]^3$ ). The primary merit of our design presented here is its large range of motion (10 mm/axis), while maintaining a compact volume ( $[150 \text{ mm}]^3$ ), as validated by experimental measurements. The contributions of this paper include (1) a review and systematic compilation of existing multi-axis parallel-kinematic designs to provide a comparison with the proposed XYZ flexure mechanism, (2) a novel exact-constraint corner assembly design that enables a practical modular fabrication and repeatable assembly of the proposed mechanism, (3) methodical design of an experimental setup that enables accurate and precise characterization of the proposed mechanism, and (4) comprehensive experimental measurements that confirm the predicted attributes of the proposed design.

This paper is organized as follows. The goals of the experimental setup design and measurement are laid out in Sec. 2. Detailed design, fabrication, and assembly of the experimental setup comprising the flexure bearings, sensors, actuators, and data acquisition are presented in Sec. 3. An overview of the experimental procedure is provided in Sec. 4. Measurement results for actuation stiffness, cross-axis error motion, actuator isolation, motion stage rotation, and lost motion are compiled in Sec. 5. This section also includes a discussion on the comparison between FEA predictions and experimental measurements. Contributions are summarized in Sec. 6.

## 2 Goals of the Experimental Setup Design

If the PFMs were ideal single-DoF constraint elements, i.e., zero stiffness and infinite motion in the DoF direction and infinite stiffness and zero motion in the DoC directions, then the performance attributes of the XYZ flexure mechanism would also be ideal.

This would imply perfect decoupling between the motion directions, perfect actuator isolation, zero cross-axis errors, zero parasitic rotations, and zero lost motion. However, in practice, the PFM is not an ideal constraint element, and therefore, “small” deviations from perfect behavior are expected. To properly characterize the XYZ flexure mechanism design, the primary challenge in the experimental setup design is to measure these “small” displacement quantities accurately and repeatably. Therefore, the experimental measurement setup has to be designed to be either free of friction and backlash or be insensitive to these effects.

For comprehensive characterization, one needs to actuate and measure along the three DoF axes simultaneously. We took advantage of the symmetry in the design to reduce the required loading conditions and measurement setups. For example, because each actuation stage has the same relative position and orientation with respect to ground and the other stages, various error motions and stiffness only need to be measured for one DoF axis for a complete set of X, Y, and Z loading conditions. Keeping this and the above-listed motion attributes in mind, the following measurement goals were identified:

- (1) Measure the actuation stiffness at the X stage for different values of X, Y, and Z actuation. The amount of variation in this actuation stiffness with varying Y and Z actuation will determine the geometric decoupling between the DoF axes.
- (2) Measure cross-axis error motions (Y and Z displacements) at the XYZ stage for different values of X actuation.
- (3) Measure parasitic rotations of the XYZ stage for different values of X, Y, and Z actuation.
- (4) Measure the actuation isolation (Y and Z displacements and X, Y, and Z rotations) at the X stage for different values of X, Y, and Z actuation.
- (5) Measure the lost motion in the X direction (difference in X displacement of the X stage and the X displacement of the XYZ stage) for different values of X, Y, and Z actuation.

These measurements require large stroke single-axis actuation at the X, Y, and Z actuation stages; large displacement measurements

along the X direction of the X stage, Y direction of the Y stage, and Z direction of the Z stage; small displacement measurements along Y and Z directions and small rotation measurements along the X, Y, and Z directions of the X stage and the XYZ stage, and X actuation force measurement at the X stage over the entire motion range of interest. This established the actuation and sensing requirements for the experimental setup design.

An additional goal in the experimental setup design was to maintain a simple fabrication and assembly process. Given the spatial design of the XYZ flexure mechanism, monolithic fabrication using traditional machining is impractical. While additive manufacturing is a possibility, metal 3D printing is still in its infancy and was not accessible to us. Instead, we set the goal to design the mechanism such that it can be assembled (from easily machinable modular components) in a repeatable manner that avoids assembly stresses and ensures consistent and precise measurements over multiple tests. Furthermore, the experimental setup was desired to be such that it can be easily reconfigured to accommodate the necessary sensors and actuators for each of the above-listed measurements.

### 3 Experimental Setup Design

The experimental setup design included the selection of dimensions and material for the flexure bearing, the design of the flexure mechanism for fabrication and assembly, and the selection and integration of actuators and sensors. A CAD rendering of the final experimental setup is shown in Fig. 2.

**3.1 Flexure Mechanism Dimensions.** The overall size, detailed dimensions, and material selection for the flexure mechanism were determined using a static yield failure criterion [4,5].

For material, aluminum 6061-T61 was selected because of its good flexural properties, phase stability, and machinability. For the desired stroke of  $\Delta = \pm 5$  mm along each primary motion direction/DoF, the first step was to select an appropriate beam length. Given the choice of PFMs as the constraint element, one of the main limiting factors is its parasitic error  $\epsilon$  ( $= 0.6D^2/L$ ), shown in Fig. 3, which results in a deviation from perfect straight-line motion [5]. In addition to contributing to cross-axis error motions in the overall flexure mechanism, this parasitic error also poses challenges in the integration of linear sensors and actuators. As discussed in Secs. 3.3 and 3.4, most large stroke linear sensors and actuators have a fixed axis of operation and do not tolerate much off-axis motion. Based on the choice of sensors and actuators used, a limit was placed on the maximum allowed off-axis motion of the actuation stage:  $\epsilon \leq 200 \mu\text{m}$ . While a large beam length  $L$  helps minimize this parasitic error, it also increases the overall mechanism size, resulting in a tradeoff. For the desired stroke and allowable error motion, the length  $L$  was chosen to be 101.6 mm (or 4 in.), which would result in an  $\epsilon$  value of approximately  $150 \mu\text{m}$ . For this length, a thickness value  $T = 0.762$  mm (or 0.030 in.) was chosen to maintain a safety factor ( $\eta$ ) of 3 against yielding. While a smaller beam thickness leads to lower

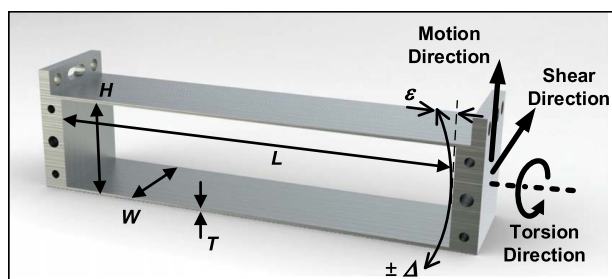


Fig. 3 PFM dimensions

maximum stress, greater stroke, and lower actuation effort, it also leads to higher parasitic rotations at the motion stage and lost motion between the actuation stage and motion stage.

Increasing the beam width  $W$  and beam separation  $H$  reduces the parasitic rotations and lost motion [5] but also leads to a larger overall mechanism size. The beam width  $W$  was chosen to be 1 in. (or 25.4 mm), which corresponds to an easily available stock plate thickness. To maintain cubic symmetry in the overall flexure mechanism, the end-to-end beam spacing must also be 25.4 mm, resulting in a center-to-center beam spacing  $H$  of 24.64 mm. It is noteworthy that, with this geometry, the PFM has relatively lower stiffness in the torsional direction compared with the shear direction (Fig. 3).

With this choice of dimensions and material, we ran FEAs in ANSYS for the overall flexure mechanism over its entire range of motion to obtain predicted values of the performance attributes listed above. The beams were modeled using SHELL181 elements, and the corner stages are modeled using the MPC184 rigid elements. The mesh density was tested and optimized for speed and precision of analysis to be a 64 by 16 mesh of square-shaped shell elements along each beam. To capture the pertinent nonlinearities, the large displacement option (NLGEOM) was turned on. Standard material properties for aluminum 6061 were assumed ( $E = 68,900 \text{ N/mm}^2$  and  $\nu = 0.33$ ). These theoretical FEA predictions were used in the selection of sensors and actuators and experimental setup design described next, and are plotted in Sec. 5 for comparison with experimental measurements.

### 3.2 Fabrication and Assembly of the Flexure Bearing.

It was desirable to construct the overall flexure mechanism with tight tolerances ( $<0.025$  mm or 0.001 in.) around the above-selected dimensions. This would ensure that the physical realization of the flexure mechanism is close to the geometry that was modeled via FEA, allowing for a meaningful comparison between experimental and FEA results. In general, it is ideal to fabricate the overall flexure mechanism monolithically, as is typically done in planar flexure designs. But, the size and spatial geometry of the proposed XYZ flexure mechanism along with the desired tight tolerances on the dimensions make monolithic fabrication very difficult in this case. For this reason, we developed an innovative modular scheme that employs 12 identical PFM units that can be easily and repeatably assembled via exact-constraint interfaces (Fig. 4). Each end of the

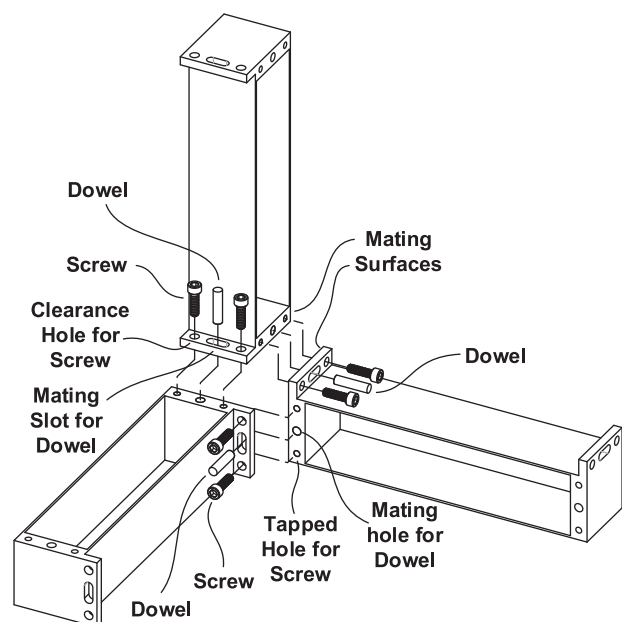


Fig. 4 Exact-constraint corner interface

PFM was designed to include alignment and assembly features: two clearance holes for screws, one mating slot for a dowel pin, two tapped holes for screws, and one mating hole for the dowel pin. At each corner of the flexure mechanism, three PFMs come together perpendicular to each other, are accurately aligned and exactly constrained using the dowel features, and securely assembled using the screws. This results in a rigid corner stage assembly without any over-constraint. This assembly process is repeated for all the eight corners. This way, all the 12 PFMs are identical and relatively simple to fabricate, and cyclic symmetry is used to achieve the desired flexure mechanism assembly.

A quick constraint analysis conveys the exact-constraint nature of this corner interface (Fig. 4). The three rigid ends of the three PFMS provide six DoF each, but since one may be treated as the reference, there are 12 DoF in all that have to be eliminated to create a joint. Each surface to surface mate eliminates three DoF; in all nine DoF are removed by three such mates. Each dowel and slot interface eliminates one DoF; in all three DoF are removed by three such mates. Thus, the assembly is left with zero DoF with respect to the reference PFM end, indicating a theoretically rigid joint. However, there is finite stiffness associated with any screwed joint, as is observed later in experimental measurements. The exact-constraint nature of each corner interface is critical to ensure that the resulting overall flexure mechanism is free of assembly stresses. The latter can alter the system mechanics and resulting motion attributes in an unpredictable manner.

The individual PFMs (shown in Fig. 3) were designed to be fabricated using standard processes. Compared with traditional machining and water-jet cutting, wire electric discharge machining (EDM) proves to be the most effective method for producing thin flexure blades while maintaining uniform thickness, tight tolerances (0.05 mm or 0.0002 in.), and low machining stresses. The various holes and slots on the two ends of the PFM were produced via a secondary machining operation on a mill. Once the 12 PFMs were fabricated, the overall flexure mechanism assembly process did not require a jig because of the in-built alignment features. The screws between the 12 PFMs were tightened sequentially and incrementally to avoid any assembly stress.

**3.3 Actuator Selection and Assembly.** For testing the performance of the XYZ flexure mechanism, we needed linear actuators that can provide large stroke (10 mm) and micron level positioning accuracy and resolution, which is adequate to demonstrate the large-range capability of the overall flexure mechanism in the three DoF directions. However, to measure the associated “small” displacements, i.e., geometric coupling, error motions, lost motion, and actuator isolation, nanometric metrology is needed as discussed in Secs. 3.4–3.6.

Several actuator options exist including manual and motorized micrometers, direct drive voice coil and moving magnet actuators, and linear motors as long they provide the desired actuation force of 30 N based on the stiffness predicted by the above FEA. A micrometer proves to be a practical and cost-effective choice that is also easy to mount and interface. In the experimental setup, each of the X, Y, and Z stages were actuated with a respective PhysikInstrumente DC motor driven micrometer (M-227.25) with an integrated rotary encoder. These actuators were operated in closed-loop using feedback from the encoder to provide a positioning accuracy of  $\pm 5 \mu\text{m}$ . Since the objective of the experiments is to vary the displacement along the primary motion directions (X, Y, and Z) over a  $\pm 5 \text{ mm}$  range, while measuring “small” deviations using non-contact sensors at the motion stages (described further below), this positioning accuracy of  $\pm 5 \mu\text{m}$  over  $\pm 5 \text{ mm}$  motion range is sufficient. Figure 5 shows the components of the X actuator sub-assembly, where the force applied at the X stage is measured using a load cell mounted between the actuator and the X stage. The load cell used was from Measurement Specialties (ELFF-T4E-20L-V10) capable of both tension and compression measurements up to 50 N with  $\pm 0.5\%$  of full-scale accuracy.

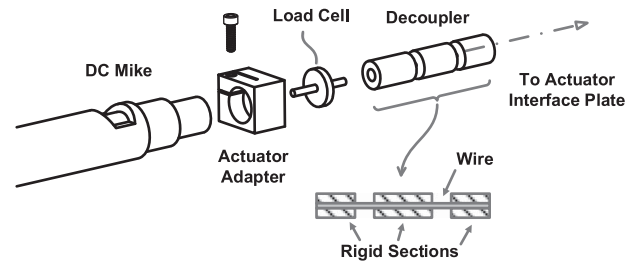


Fig. 5 X actuator sub-assembly with load cell

The micrometer was attached to the load cell through a custom designed *actuator adapter* that clamps on to the tip of the micrometer on one side and is screwed to the load cell on the other end (Fig. 5). Next, a *decoupler* was employed to connect the load cell to the X actuation stage corner assembly (described in Sec. 3.5) to transmit the actuation force along the actuation direction while isolating the micrometer and load cell from the off-axis motions of the X actuation stage (e.g.,  $150 \mu\text{m}$  Y displacement, described above). The decoupler is constructed from three rigid sections connected by two piano wires. The length and thickness of the flexible sections were chosen based on buckling and yield criteria for the expected loads (30 N) with a safety factor of 2. The axial stiffness of the decoupler is designed to be at least an order of magnitude higher than the transmission stiffness of the flexure mechanism in any given primary motion direction. This decoupler interfaces with the flexure mechanism via an *actuator interface plate* described in Sec. 3.5.

The actuators are mounted on the base plate via respective *actuator mounts* that are aligned to the base plate via dowel pins and secured using screws (Fig. 2). The actuator mounts are sized such that the maximum expected actuation force will not deflect the mount by more than 0.1% of the actuation range, or  $\pm 5 \mu\text{m}$ , in the direction of actuation.

**3.4 Primary Direction Sensors and Assembly.** High-resolution linear optical encoders are well-suited for measuring long-range single-axis translations of the X, Y, and Z stages. Renishaw encoders (RELM scale, Si-HN-4000 read-head, and SIGNUM interface) provide 80 mm measurement range and allow off-axis tolerance of  $250 \mu\text{m}$ , which is greater than the expected off-axis motion of  $150 \mu\text{m}$  at the actuation stages. This sensor provides 5 nm resolution, which is more than adequate for the DoF displacement measurement given a positioning accuracy is  $\pm 5 \mu\text{m}$ . The encoder strips are mounted on respective actuation stages via a *corner assembly* shown in Fig. 6. The corresponding read-heads are mounted on *encoder mounts* that are connected to the base plate, as shown in Fig. 2. The encoder mounts are aligned and connected to the base plate in a manner similar to the

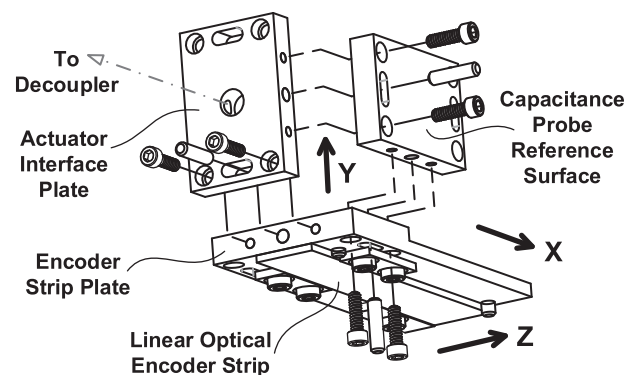


Fig. 6 X stage corner assembly

actuator mounts but are relatively smaller in size because they do not need to bear loads like the actuator mounts. The encoder read-heads are attached to the encoder mounts via two screws and aligned via tight-tolerance machined features.

**3.5 X Stage Corner Assembly.** The X, Y, and Z actuation stages need interface features that allow for the transmission of positive and negative direction actuation forces. Additionally, the X actuation stage also needs to be equipped with sensor interfaces to measure actuation isolation. To accommodate these requirements in the relatively tight space provided by the flexure mechanism corners and maintain precise and repeatable alignment, a corner assembly is designed using the same exact-constraint alignment and mating features that are built into the PFM units. Figure 6 shows an exploded view of the X stage corner assembly. The *actuator interface plate* connects with the X actuator via the *decoupler* shown in Fig. 5. Given the symmetry of the XYZ flexure mechanism design, the error motions associated with an actuation stage (i.e., actuator isolation) are measured at the X stage only. Since these error motions are relatively small ( $\leq 150 \mu\text{m}$ ), an arrangement of five capacitance probes is used to measure the Y and Z translations and the three rotations at the X stage. Three capacitance probes aligned in the Z direction measure with respect to a *reference surface* that is part of the X stage corner assembly. Another two cap probes aligned in the Y direction measure with respect to one of the machined faces of the vertical PFM at the X stage. Lion Precision capacitive probes (model # C1A), capable of 10 nm resolution over 500  $\mu\text{m}$  range, were selected for this purpose. The capacitance probes are mounted in precision-reamed, C-clamp style holes that are part of a *cap probe mount*, aligned and attached to the base plate (Fig. 2). The maximum relative rotation between the probe and a target at either the X stage or the XYZ stage is accounted for and shown to produce a relatively small measurement error (see Sec. 5.5). The X-axis linear optical encoder strip is mounted on the *encoder strip plate*. A similar assembly is also used to mate the Y and Z stage actuators and encoders with the flexure mechanism.

**3.6 XYZ Stage Sensor Assembly.** The cross-axis errors and parasitic rotations at the XYZ stage are measured using multiple capacitance probes, same as the ones mentioned above. Sensing these motions requires additional consideration because the XYZ stage exhibits large-range motion in all three DoF unlike the actuation stages that have large motion only along one respective DoF. A multi-axis parallel mirror laser interferometry system is ideally suited for such displacement measurements due to its ability to precisely record displacement along any given DoF axis even in the presence of large-range, off-axis motions. Since we did not have access to such a laser interferometry system, a sensing system comprising three capacitance probes was designed to accommodate the large range and large off-axis motions of the XYZ stage. Figure 7 provides an exploded view of the XYZ stage sensor assembly. The three probes are mounted on a *linear guide* driven by a *manual micrometer*. The linear guide is mounted on the *XYZ stage sensor mount*, which in turn is aligned and attached to the base plate. The position of this linear guide (and therefore, the capacitance probes) with respect to the mount (and therefore the base plate) is measured using a linear encoder, with an *encoder strip* attached to the linear guide and an *encoder read-head* attached to the sensor mount. This linear encoder is same make and model as those used on the X, Y, and Z actuation stages.

This same modular sensor assembly is used in two configurations, one at a time (both shown in Fig. 2). In the first configuration, the mount is attached to the base plate such that the three capacitance probes point in the Z direction. Thus, for a fixed actuation along the Z-axis, the other two actuators can be cycled over their full range without interfering with the probes, which measure Z translation and X and Y rotations of the XYZ stage. For a different fixed value of Z actuation, the micrometer is adjusted to locate the

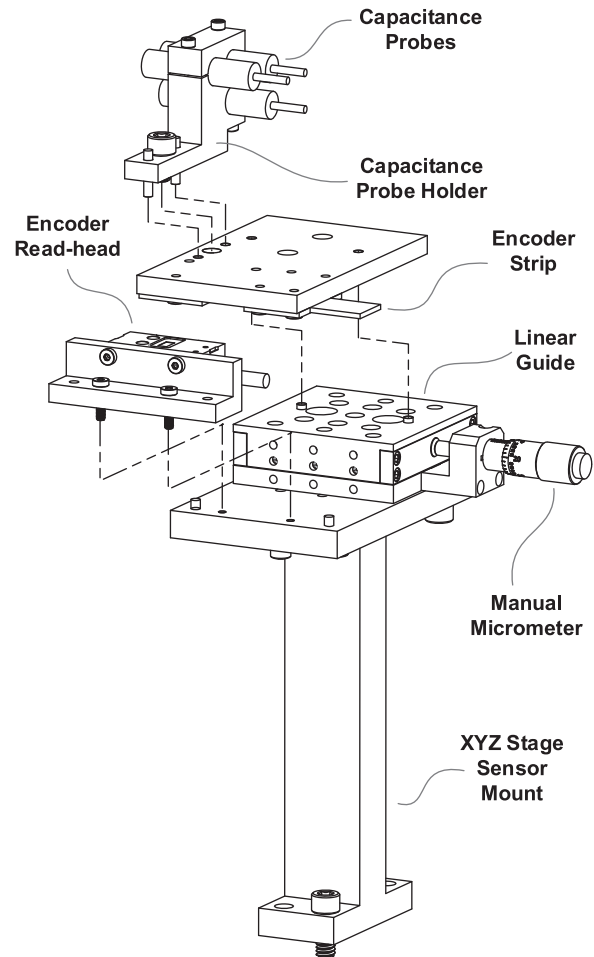


Fig. 7 XYZ stage sensor assembly

three probes at a new Z position, which is measured by the linear encoder, and the experiment is repeated by cycling X and Y actuators over their full range. This helps record the Z direction lost motion and the X and Y rotations of the XYZ stage over the entire X, Y, and Z actuation range.

In the second configuration of the XYZ stage sensor assembly, the three capacitance probes measure along the X-axis, while the X actuation remains fixed and the Y and Z actuators are cycled through their full ranges. This helps capture the X direction lost motion of the XYZ stage relative to the X stage, as well as the Y and Z rotations of the XYZ stage. This experiment is repeated for multiple discrete values of X actuation, while adjusting the X location of the three capacitance probes using the micrometer and measuring this location using the linear encoder.

## 4 Experimental Procedure

The experimental hardware designed, fabricated, and assembled, as described in Sec. 3, is shown in Fig. 8. With this experimental hardware, five different sensor setups and testing procedures were employed for measurement goals (1) through (5) listed in Sec. 2. In each of the five test setups, the three linear optical encoders measure the X, Y, and Z displacements of the corresponding actuation stages, and the load cell measures the actuation force on the X actuation stage. However, capacitance probes are moved between five mounting locations, described next, resulting in five sensor setups:

- (a) In this setup, all capacitance probes are removed from the experiment. A linear encoder measures the X displacement

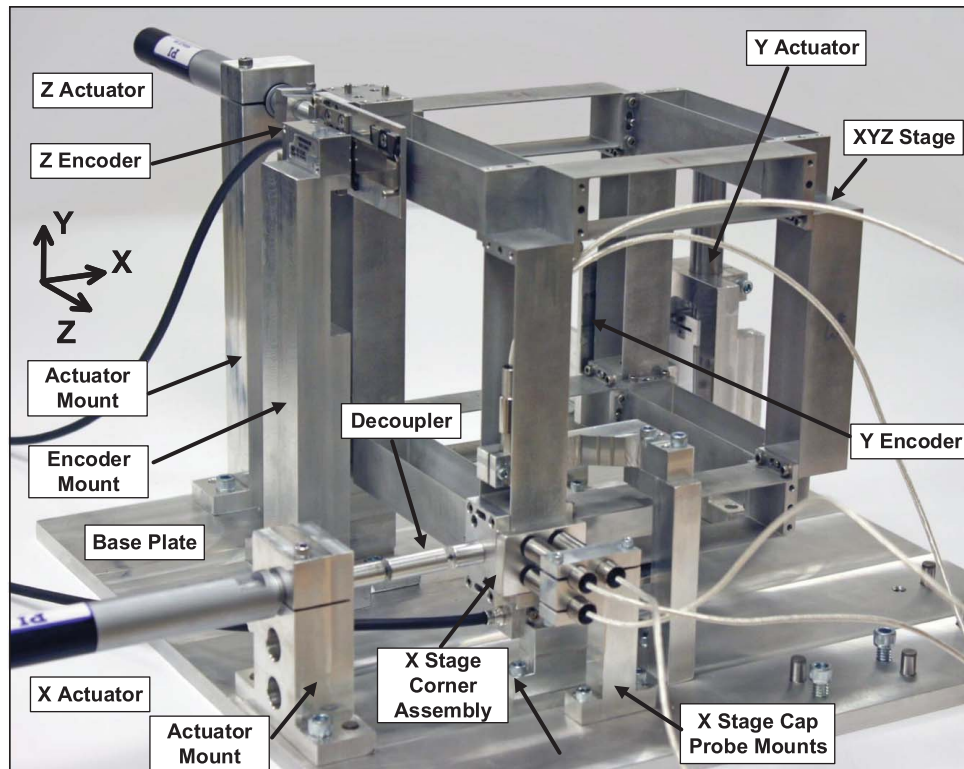


Fig. 8 Experimental hardware: sensor setup (c) and (d)

of the X stage for various combinations of X, Y, and Z actuation to address measurement goal (1) large range due to geometric decoupling.

- (b) Three probes are mounted at the XYZ stage in the X direction to measure its X translation and Y and Z rotations, for various combinations of X, Y, and Z actuation. This addresses measurement goals (3) parasitic rotations and (5) lost motion.
- (c) Two probes are mounted at the X stage in the Y direction to measure the Y translation and Z rotation for various combinations of X, Y, and Z actuation. This captures measurement goal (4) actuation isolation.
- (d) Three probes are mounted at the X stage in the Z direction to measure the Z translation and X and Y rotations for various combinations of X, Y, and Z actuation. This further addresses the measurement goal of (4) actuation isolation.
- (e) Three probes are mounted at the XYZ stage in the Z direction to measure the Z translation and X and Y rotations for various combinations of X and Y actuation. This setup addresses the measurement goals (2) cross-axis error motion and (3) parasitic rotations.

The experimental setup was designed for testing over an X, Y, and Z motion range of  $\pm 5$  mm. The testing using test setup (a) indeed confirmed this motion range in each direction. However, upon running the experiments, it became evident that the rotational error motions of the X, Y, and Z stages caused the respective linear optical encoders at these stages to lose angular alignment between the read-head and the encoder strip before the full  $\pm 5$  mm range was reached. Therefore, some of the tests were limited to a maximum range of  $\pm 2.5$  or  $\pm 3$  mm per direction.

## 5 Results and Discussion

In this section, we present a graphical and quantitative comparison between FEA predictions and experimental measurements for various actuation conditions. While reporting the results in the

following paragraphs and figures, we follow a nomenclature in which the super-script represents the rigid stage being considered and the sub-script represents the relevant direction of displacement, rotation, or force associated with this stage. For example,  $U_x^Y$  represents the X direction displacement of the Y stage,  $\theta_y^Z$  represents the Y direction rotation of the Z stage,  $F_z^X$  represents the Z direction force on the X stage, and so on.

In the following figures, FEA results are displayed using black lines and the experimental data are displayed with blue markers and polynomial fit lines.

**5.1 Primary Motion Direction Stiffness.** Test setup (a) was used to measure the primary motion direction stiffness. Figure 9 shows the stiffness associated with the X direction displacement

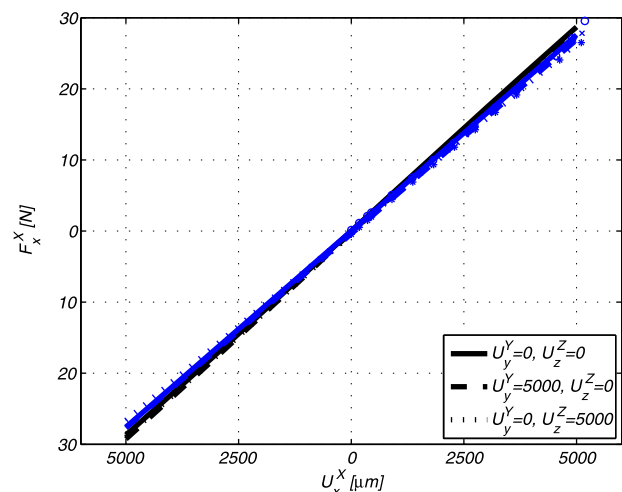


Fig. 9 Direction force-displacement relation

of the X stage in response to an X direction force at this stage. This X direction stiffness is measured for various combinations of Y and Z actuation. The force–displacement curves are linear, as expected, and the measured stiffness is within 7% of the predicted stiffness. Furthermore, FEA and experimental measurements reveal predominantly linear behavior and minimal variance in this X direction stiffness for all combinations of Y and Z actuation. This confirms the absence of over-constraint in the motion directions and the high degree of decoupling between these motion directions, thus enabling large motion range.

There is no measurable variation in the X direction stiffness with respect to Y actuation and small variation (<3%) with respect to Z actuation. X direction stiffness comes from bending of the green PFMs; while Y actuation does not load the green PFM, the Z actuation loads these green PFM in shear resulting in a slight drop in their bending stiffness.

**5.2 Lost Motion.** Test setup (b) was used to measure lost motion. In Fig. 10, the difference between  $U_x^{XYZ}$  and  $U_x^X$ , i.e., the motion that is “lost” between the point of actuation (X stage) and the point of interest (XYZ stage) is plotted with respect to Y actuation for different values of X actuation. Because this lost motion is largely insensitive to the Z actuation, as corroborated in Sec. 5.3, the curves are plotted for  $U_z^Z = 0$  mm.

The X direction lost motion versus  $U_y^Y$  plots show both quadratic and linear components. The quadratic component, which is the same in both the experimental measurement and the FEA, is the kinematic term that arises from the arc-length conservation of the red PFMs (parasitic error  $\varepsilon$  shown in Fig. 3). The linear component arises due to a moment from Y actuation force about the Z-axis, resulting in the torsion of the green PFMs. The green PFMs have relatively low torsional stiffness, while the blue PFMs have a relatively high axial stiffness (see Fig. 3). Since the Y stage does not correspond to the Center of Stiffness location of the mechanism with respect to Y actuation, which instead lies close to the center of the plane formed by Ground-Y-XY-X stages, a positive direction Y actuation at the Y stage causes the plane formed by the X-XZ-XYZ-XY stages to rotate about the Z-axis. This rotation causes the X stage to have a translational component in the positive X direction and the XYZ stage to have a translational component in the negative X direction, resulting in additional lost motion. This produces the linear elastic component seen in X direction lost motion versus  $U_y^Y$  plots. Furthermore, the slope of the linear component is higher in the experimental measurement compared with FEA. There are two likely sources for this discrepancy. First, the torsional stiffness of the PFM is sensitive to thickness and flatness of the constituent flexure beams and,

therefore, can be lower in practice compared with ideal. Second, there is finite joint stiffness of each corner assembly in the assembled experimental hardware, whereas these joints are modeled as ideal (i.e., infinitely stiff) in the FEA.

Furthermore, the lost motion varies nearly linearly with  $U_x^X$ , also indicated in Fig. 10. Similar to the phenomenon described above, the application of an X actuation force at the X stage results in a torsional moment on the green PFMs about the Z-axis. The resulting torsion of the green PFMs causes the plane formed by the X-XZ-XYZ-XY stages to rotate about the Z-axis. Since the blue PFMs are stiff in shear, they deform relatively less during this rotation. This rotation about the Z-axis produces an additional displacement in the positive X direction at the X stage and a similar displacement in the negative X direction at the XYZ stage, thereby further contributing to lost motion. This torsion moment, which increases linearly with the applied X actuation, is a consequence of the fact that the Center of Stiffness of this mechanism with respect to X actuation does not lie at the X stage and instead lies close to the center of the plane formed by the Ground-X-XZ-Z stages. As indicated above, this linear elastic component due to X actuation is higher in the experimental measurement compared with FEA due to the finite joint stiffness of the corner assemblies and lower torsional stiffness of the PFMs.

Overall, the X direction lost motion measurement varies from  $528 \mu\text{m}$  when  $U_x^X$  is  $-2500 \mu\text{m}$  and  $U_y^Y$  is  $-2500 \mu\text{m}$  to  $-550 \mu\text{m}$  when  $U_x^X$  is  $2500 \mu\text{m}$  and  $U_y^Y$  is  $2500 \mu\text{m}$ . This may be extrapolated to  $925 \mu\text{m}$  when  $U_x^X$  is  $-5000 \mu\text{m}$  and  $U_y^Y$  is  $-5000 \mu\text{m}$ , and  $-1125 \mu\text{m}$  when  $U_x^X$  is  $5000 \mu\text{m}$  and  $U_y^Y$  is  $5000 \mu\text{m}$ .

**5.3 Cross-Axis Error Motion.** Test setup (e) was used to measure cross-axis error motion, which represents the motion of the XYZ stage in a direction other than the actuated direction when the latter is held fixed. For X actuation fixed ( $U_z^Z = 0$ ), the displacement of the XYZ stage in the X direction in response to Y and Z actuations is illustrated in Fig. 11. By definition, this cross-axis error motion is correlated to the X direction lost motion, which explains the similarities between Figs. 10 and 11. In fact, Fig. 10 shows that for various fixed values of X actuation ( $U_x^X$ ), the variation of  $U_x^{XYZ}$  with respect to  $U_y^Y$  remains the same. As a result, the cross-axis error in Fig. 11 is plotted for  $U_x^X = 0$  mm only, but for various values of Y and Z actuation.

The linear and quadratic components in these plots are the same as explained in Sec. 5.2. Also, while the quadratic component matches well between the FEA and experiments, while the linear component is higher in the experiments due to the finite joint stiffness in the hardware. The cross-axis error motion in X direction varies from a maximum measured value of  $264 \mu\text{m}$  when  $U_y^Y$  is

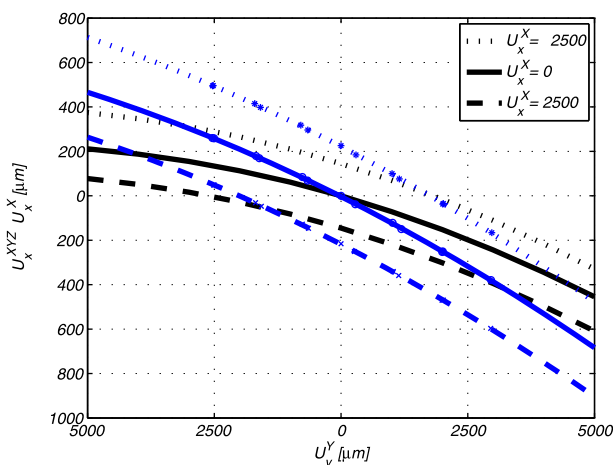


Fig. 10 X direction lost motion versus  $U_y^Y$

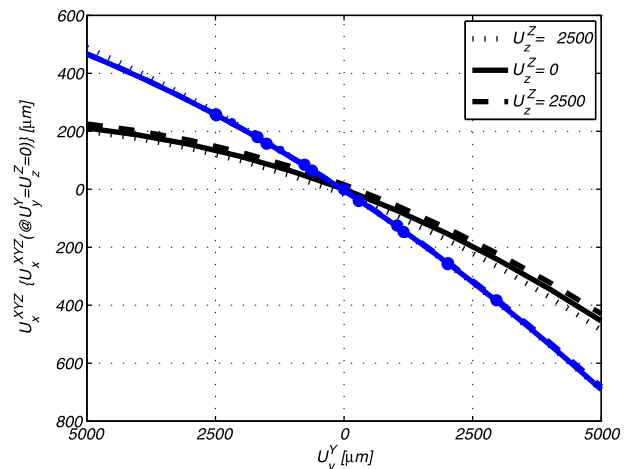


Fig. 11 X direction cross-axis error motion

$-2500 \mu\text{m}$  and  $U_z^Z$  is  $-2500 \mu\text{m}$  to  $-388 \mu\text{m}$  when  $U_y^Y$  is  $3000 \mu\text{m}$  and  $U_z^Z$  is  $2500 \mu\text{m}$ . These numbers can be extrapolated to cross-axis error motion in X direction that varies from a maximum value of  $470 \mu\text{m}$  when  $U_y^Y$  is  $-5000 \mu\text{m}$  to  $-690 \mu\text{m}$  when  $U_y^Y$  is  $5000 \mu\text{m}$ . Also, these measurements are largely invariant with Z actuation as evident from the overlapping blue lines corresponding to  $U_z^Z = -2500, 0,$  and  $2500 \mu\text{m}$ . This insensitivity to Z actuation is due to the high axial stiffness of the green PFM and high shear stiffness of the red PFM. This is also why the lost motion plotted in Sec. 5.2 is insensitive to Z actuation.

**5.4 Actuator Isolation.** Actuator isolation in a multi-axis flexure mechanism ensures that the point of actuation in any given direction moves only in that direction and is not influenced by actuation in the other directions. Test setup (c) was used to measure X actuator isolation in the Y direction, for different values of Y and Z actuation. Figure 12 plots the Y direction displacement of the X stage ( $U_y^X$ ) against Z actuation ( $U_z^Z$ ) for different values of Y actuation ( $U_y^Y$ ). Since X actuation has a minimal impact on the Y motion of the X stage ( $U_y^X$ ), these curves are plotted for  $U_x^X = 0 \text{ mm}$  only. A Z actuation loads the green PFMs, particularly G1, in shear in the Y direction. This shear stiffness is relatively high in theory and largely linear, with slight nonlinearity at larger loads as indicated by the FEA results (black lines) in Fig. 12. In practice, this shear stiffness is sensitive to any deviation from perfectly planar geometry of the flexure beams of the green PFM [6]. Consequently, the experimental measurements indicate a lower than ideal stiffness.

The maximum measured Y direction motion of the X stage is  $85 \mu\text{m}$  when  $U_y^Y$  is  $2500 \mu\text{m}$  and  $U_z^Z$  is  $-2500 \mu\text{m}$ , and  $-100 \mu\text{m}$  when  $U_y^Y$  is  $2500 \mu\text{m}$  and  $U_z^Z$  is  $3000 \mu\text{m}$ . This extrapolates to a maximum Y direction motion of the X stage of  $172 \mu\text{m}$  when  $U_z^Z$  is  $-5000 \mu\text{m}$  and  $-160 \mu\text{m}$  when  $U_z^Z$  is  $5000 \mu\text{m}$ . The FEA and experimental measurements both show a relative insensitivity to Y actuation because the Y actuation force does not load the green PFMs in shear the way the Z actuation force does.

Test setup (d) is used to measure X actuator isolation in the Z direction. Figure 13 shows the Z direction displacement of the X stage ( $U_z^X$ ) over the entire range of X actuation ( $U_x^X$ ). Since this motion is found to be largely insensitive to both Y and Z actuations, the curve is plotted for Y and Z actuations held at  $0 \text{ mm}$ . The Z direction displacement of the X stage ( $U_z^X$ ) is primarily due to the kinematic arc-length conservation of the green PFMs (parasitic error  $\epsilon$  shown in Fig. 3) and, therefore, has a quadratic dependence on the X direction displacement of the X stage. The behavior is well characterized with a good agreement between the experimental measurement and FEA. The maximum measured Z direction motion of the X stage is  $-47.8 \mu\text{m}$  when  $U_x^X$  is  $3000 \mu\text{m}$ . This

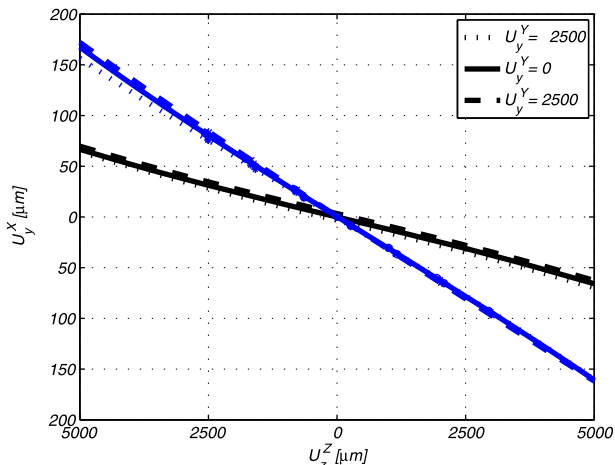


Fig. 12 X actuator isolation (Y direction)

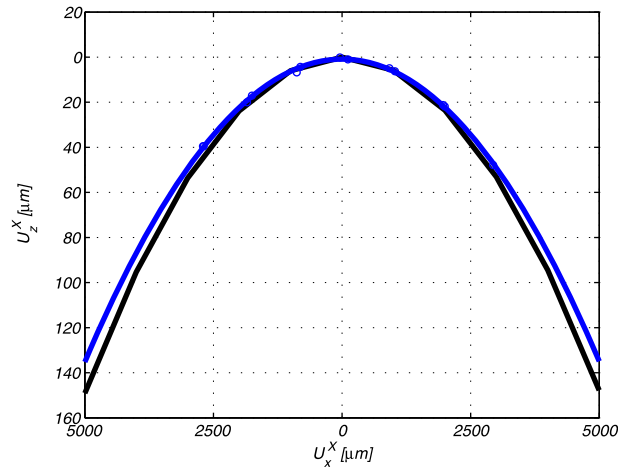


Fig. 13 X actuator isolation (Z direction)

may be extrapolated to a maximum Z direction motion of the X stage of  $-135 \mu\text{m}$  when  $U_x^X$  is  $\pm 5000 \mu\text{m}$ .

**5.5 XYZ Stage Rotations.** Test setup (e) was used to measure XYZ stage rotations about the X direction ( $\theta_x^{XYZ}$ ) against Y actuation for three different Z actuations (Fig. 14). The rotation varies primarily with Y and Z actuations, which produce moments about the X direction at the XYZ stage. It is largely insensitive to X actuation because the X direction force does not produce such a moment. Therefore, the curves are plotted for  $U_x^X$  held at  $0 \text{ mm}$ .

Since the Z stage does not correspond to the Center of Stiffness of the mechanism with respect to Z actuation, the latter causes the XYZ stage to rotate about the X-axis due to the rotational bending stiffness of the blue PFM. This relationship is largely linear because the CoS location remains invariant with increasing Z actuation and the rotational bending stiffness of the blue PFMs is linear with increasing displacement.

Similarly, because the Y actuation happens at the Y stage, which is not the Center of Stiffness of mechanism for this actuation direction, it results in a positive moment about the X-axis. Given the relatively lower torsional stiffness of the red PFM, this results in the plane formed by the Y-YZ-XYZ-XY stages to rotate about the X direction. Since this torsional stiffness is largely constant but reduces slightly with increasing displacement, a small nonlinearity may be seen in Fig. 14.

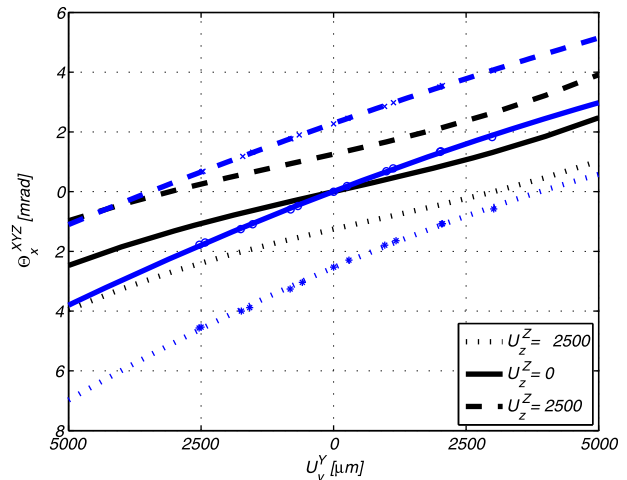


Fig. 14 X direction rotation of the XYZ stage



The maximum measured X direction rotation of the XYZ stage is  $-4.6$  mrad when  $U_y^Y$  is  $-2500 \mu\text{m}$  and  $U_z^Z$  is  $-2500 \mu\text{m}$  and  $4$  mrad when  $U_y^Y$  is  $-3000 \mu\text{m}$  and  $U_z^Z$  is  $2500 \mu\text{m}$ . This extrapolates to a maximum X direction rotation of the XYZ stage of  $-9.5$  mrad when  $U_y^Y$  is  $-5000 \mu\text{m}$  and  $U_z^Z$  is  $-5000 \mu\text{m}$  and  $7.5$  mrad when  $U_y^Y$  is  $5000 \mu\text{m}$  and  $U_z^Z$  is  $5000 \mu\text{m}$ . Because of design symmetry, the XYZ stage rotation about the Y direction ( $\theta_y^{XYZ}$ ) depends similarly on the X and Z actuation but not as much on the Y actuation. And, the XYZ stage rotation about the Z direction ( $\theta_z^{XYZ}$ ) depends on the X and Y actuation but not as much on the Z actuation.

Also, it can be shown [19] that the impact of the maximum measured stage rotation ( $-4.6$  mrad) on the accuracy of the capacitance probe measurement is less than  $1.27 \mu\text{m}$  over displacement measurements that are hundreds of microns as seen in Figs. 10–13. This represents a less than 1% accuracy error for the capacitance probe, which is adequate for the experimental validation presented above.

## 6 Summary and Conclusions

The experimentally determined motion performance of the proposed XYZ flexure mechanism, comparison with FEA, and future design insights are summarized next.

- (1) The experiments confirm  $10$  mm (or  $\pm 5$  mm) motion range in each direction, with very little stiffness variation ( $<3\%$ ) in the presence of actuation along the other directions. This corroborates the constraint-based design of the XYZ flexure mechanism to avoid over-constraint in the motion directions and enable large motion range.
- (2) Lost motion per axis is within  $915 \mu\text{m}$  and  $-1125 \mu\text{m}$  over the entire motion range in X-, Y-, Z directions (i.e., 20.4% of range). The key design drivers for this are relatively low torsion stiffness of the PFMs, application of actuation forces away from the Center of Stiffness of the mechanism, and finite joint stiffness of the corner assemblies. In future optimized designs, the torsional stiffness of the PFM may be improved by using reinforced beams and more than two beams and/or greater beam width. If this XYZ flexure mechanism is used as part of a positioning stage, then appropriate extensions can be incorporated to ensure that actuation forces are applied at the Center of Stiffness of the mechanism. Furthermore, the corner assembly can be designed with larger size screws that can ensure greater joint pre-load and therefore greater joint stiffness.

- (3) Cross-axis error is within  $470 \mu\text{m}$  and  $-690 \mu\text{m}$  over the entire range in all motion directions, which corresponds to 11.6% of range. The sources of cross-axis error are the same as those for lost motion, and therefore, the design considerations mentioned above are relevant here as well. Additionally, in a positioning stage application, lost motion and cross-axis error can be addressed by feedback control that employs end-point sensing at the XYZ stage.
- (4) Actuator isolation is within  $\pm 170 \mu\text{m}$  over the entire range in all motion directions, which corresponds to 3.3% of range. For a positioning stage application, such low values of actuator isolation is critical to be able to incorporate large-range single-axis actuators.
- (5) Parasitic rotations of the XYZ stage are within  $-9.5$  mrad and  $7.5$  mrad over the entire range in all motion directions. Since these rotations are in non-actuated directions, it is critical to further minimize them via design. This can be accomplished by increasing the torsional stiffness of the PFM and by actuating at the Center of Stiffness of the mechanisms (as noted above).

Further details on the design of the proposed XYZ flexure mechanism, experimental setup, and measurement methods and results may be found in Ref. [7]. Now that the motion attributes and performance of the proposed XYZ flexure mechanism have been validated via FEA and experiments, future work involves utilizing this mechanism in the design of an XYZ positioning system for applications in high-precision metrology and manufacturing. This will involve considerable design optimization of the size, shape, and geometry of the flexure mechanism, selection and integration of suitable sensors and actuators suitable for the application, control system design and implementation, and a mechatronic integration to achieve the desired positioning performance driven by the application.

### Conflict of Interest

There are no conflicts of interest.

### Data Availability Statement

The datasets generated and supporting the findings of this article are obtainable from the corresponding author upon reasonable request.

## Appendix: Literature Review

**Table 1 Literature review: 3 DoF parallel kinematic XYZ flexure mechanisms**

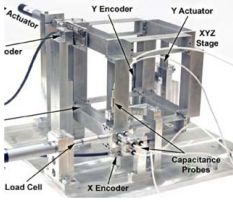
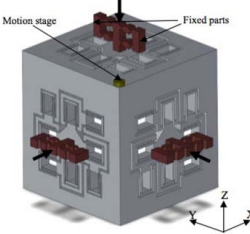
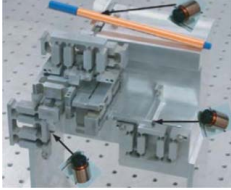
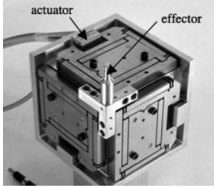
Design	Size	Motion range	Cross-axis error	Actuator isolation	Parasitic rotations	Experimental hardware
Awtar et al. [1] Ustick [7]—This paper 	~150 mm × 150 mm × 150 mm	10 mm × 10 mm × 10 mm Kinematic decoupling between axes	<11.6% of range	<3.3% of range	9.5 mrad over entire motion range	Wire EDM, milling, precision exact-constraint assembly. Comprehensive experimental measurements. Mtl: Aluminum 6061
Hao and Kong [8] 	~300 mm × 300 mm × 300 mm	9.5 mm × 9.5 mm × 9.5 mm Kinematic decoupling between axes	Theoretical prediction: <1% of motion range	Theoretical prediction of perfect actuator isolation. Small but finite values expected in practice.	Theoretical prediction of zero rotation. Small but finite value expected in practice.	Theoretical design with no experimental validation. Challenges in assembly and very large motion stage. Mtl: Aluminum 6061
Tang and Chen [9] 	~300 mm × 150 mm × 200 mm	1 mm × 1 mm × 1 mm Kinematic decoupling between axes	<1.9% of motion range	Not reported. Nominally small but finite value expected.	<1.5 mrad claimed without experimental data.	Wire EDM and mechanical assembly. Limited experimental validation data. Mtl: Aluminum 7075
Bacher et al. [10] 	~100 mm × 100 mm × 100 mm	2 mm × 2 mm × 2 mm Kinematic decoupling between axes	Not reported. Nominally small but finite value expected due to decoupled design.	Not reported. Nominally small but finite value expected due to decoupled design.	Not reported. Nominally small but value expected due to decoupled design.	Wire EDM and mechanical assembly. No experimental measurements reported. Mtl: Steel X220CrVMo13-4

Table 1 Continued

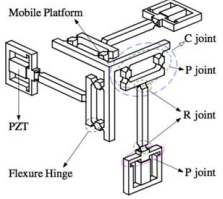
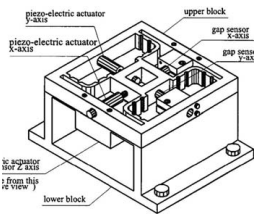


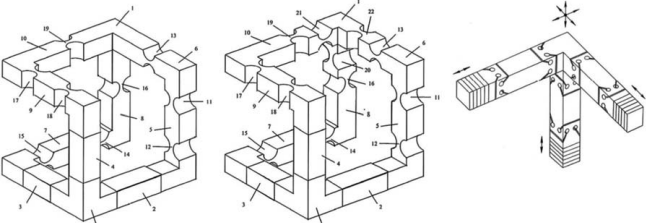
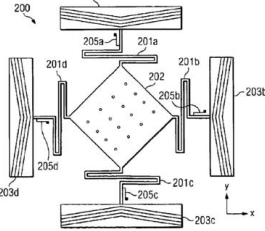
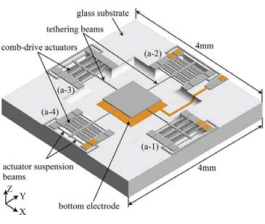
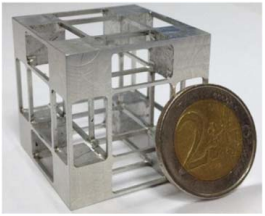
Design	Size	Motion range	Cross-axis error	Actuator isolation	Parasitic rotations	Experimental hardware
Li and Xu [11] 	~45 mm × 45 mm × 45 mm	140 μm × 140 μm × 140 μm Kinematic decoupling between axes	Not reported. Nominally small but finite value expected due to decoupled design.	Not reported. Nominally small but finite value expected due to decoupled design.	Not reported. Rotational over-constraint should lead to nominally small rotations.	Theoretical design with no experimental validation. Challenges in assembly and large motion stage. Mtl: Titanium alloy Ti-6Al-4V
Ku et al. [12] 	Not reported. Estimated: ~120 mm × 120 mm × 70 mm	3.2 μm (X) × 5 μm (Y) × 3.5 μm (Z) Small range due to inadequate kinematic decoupling.	Not reported. Nominally small but finite value expected due to symmetric design in XY.	Not reported. Nominally large value expected due to inadequate kinematic decoupling.	Not reported. Nominally large value expected due to inadequate rotational constraints	Planar flexure design can be readily fabricated via Wire EDM, followed by some assembly. Limited experimental validation of static motion attributes. Mtl: Not reported
Yao et al. [13] 	Not reported. Estimated: ~25 mm diameter × 7 mm height	Max 87 μm along each axis. Overall work volume: 3.223 × 10 <sup>4</sup> μm <sup>3</sup>	Not reported. Nominally large without feedback control due to lack of kinematic decoupling between X, Y, and Z axes.	Not reported. Nominally small but finite value expected due to kinematic decoupling between three actuators.	Not reported. Rotational over-constraint should lead to nominally small rotations.	Wire EDM and mechanical assembly. Limited experimental validation of static motion attributes. Mtl: ANSI 1045 steel
Koseki et al. [14] 	Not reported. Estimated: ~15 mm diameter × 25 mm height	Not reported. Estimated <100 μm	Not reported. Nominally large without feedback control due to lack of kinematic decoupling between X, Y, and Z axes.	Not reported. Nominally small but finite value expected due to kinematic decoupling between three actuators.	Experimental data not reported. Rotational over-constraint should lead to nominally small rotations.	Additive manufacturing. Limited experimental validation data. Mtl: Epoxy resin

Table 1 Continued

Design	Size	Motion range	Cross-axis error	Actuator isolation	Parasitic rotations	Experimental hardware
Parikian [15], Arakelian [16] 						
		Kinematically decoupled XYZ flexure mechanism concepts. Size and range not reported. Range expected to be small given the use of notch flexures.	Cross-axis coupling, actuator isolation and rotations expected to be nominally small but finite.	Wire EDM and mechanical assembly possible. No theoretical or experimental validation data.		
Sarkar et al. [17] 	$\sim 1 \text{ mm} \times 1 \text{ mm}$ footprint	Not reported. Estimated $\sim$ tens of $\mu\text{m}$ in X and Y, and a few $\mu\text{m}$ in Z.	Not reported. Nominally small but finite value expected due to symmetric design in XY.	Not reported. Nominally small but finite value expected due to kinematic decoupling between three actuators.	Not reported. Nominally large value expected due to inadequate rotational constraints	Micro-ElectroMechanical System (MEMS) fabrication. No theoretical or experimental validation data. Mtl: Silicon
Liu et al. [18] 	$\sim 4 \text{ mm} \times 4 \text{ mm}$ footprint	$25 \mu\text{m} \times 25 \mu\text{m} \times 3.5 \mu\text{m}$	$<9\%$ of motion range for X and Y actuation, and $<5\%$ for Z	Not reported. Nominally small but finite value expected due to kinematic decoupling between three actuators.	Not reported. Nominally large value expected due to inadequate rotational constraints	Micro-ElectroMechanical System (MEMS) fabrication. Limited experimental validation data. Mtl: Silicon
Hao [2] and Li and Hao [3] 	$35 \text{ mm} \times 35 \text{ mm} \times 35 \text{ mm}$ [2] $\sim 100 \text{ mm} \times 100 \text{ mm} \times 100 \text{ mm}$ [3]	$\sim 0.6 \text{ mm} \times 0.6 \text{ mm} \times 0.6 \text{ mm}$	$<2.2\%$ of range	$<1.35\%$ of range	$0.12 \text{ mrad}$ over entire motion range	Traditional machining (CNC) and assembly. Mtl: Aluminum 1050

## References

- [1] Awtar, S., Ustick, J., and Sen, S., 2012, "An XYZ Parallel-Kinematic Flexure Mechanism With Geometrically Decoupled Degrees of Freedom," *ASME J. Mech. Rob.*, **5**(1), p. 015001.
- [2] Hao, G., 2013, "Towards the Design of Monolithic Decoupled XYZ Compliant Parallel Mechanisms for Multi-Function Applications," *Mech. Sci.*, **4**, pp. 291–302.
- [3] Li, H., and Hao, G., 2017, "Constraint-Force-Based Approach of Modelling Compliant Mechanisms: Principle and Application," *Precis. Eng.*, **47**, pp. 158–181.
- [4] Howell, L., 2001, *Compliant Mechanisms*, John Wiley & Sons, Hoboken, NJ.
- [5] Smith, S., 2000, *Flexure: Elements of Elastic Mechanisms*, Gordon & Breach, CRC Press.
- [6] Nijenhuis, M., Meijaard, J. P., Mariappan, D., Herder, J. L., Brouwer, D. M., and Awtar, S., 2017, "An Analytical Formulation for the Lateral Support Stiffness of a Spatial Flexure Strip," *ASME J. Mech. Des.*, **139**(5), p. 051401.
- [7] Ustick, J., 2012, *Design, Fabrication, and Experimental Characterization of a Large Range XYZ Parallel Kinematic Flexure Mechanism*, M.S., University of Michigan, Ann Arbor, MI.
- [8] Hao, G., and Kong, X., 2009, "A 3-DOF Translational Compliant Parallel Manipulator Based on Flexure Motion," ASME IDETC, pp. 101–110.
- [9] Tang, X., and Chen, I.-M., 2006, "A Large-Displacement and Decoupled XYZ Flexure Parallel Mechanism for Micromanipulation," IEEE International Conference on Automation Science and Engineering, Shanghai, China, Oct. 8–10, IEEE, pp. 73–78.
- [10] Bacher, J.-P., Bottinelli, S., Breguet, J.-M., and Clavel, R., 2001, "Delta: Design and Control of a Flexure Hinges Mechanism," *Microrobotics and Microassembly III*, Oct. 29–30, pp. 135–142.
- [11] Li, Y., and Xu, Q., 2005, "Kinematic Design of a Novel 3-DOF Compliant Parallel Manipulator for Nanomanipulation," Proceedings of the 2005 IEEE/ASME International Conference on Advanced Intelligent Mechatronics, Monterey, CA, July 24–28, pp. 93–98.
- [12] Ku, S.-S., Pinsopon, U., Cetinkunt, S., and Nakajima, S.-i., 2000, "Design, Fabrication, and Real-Time Neural Network Control of a Three-Degrees-of-Freedom Nanopositioner," *IEEE/ASME Trans. Mechatron.*, **5**(3), pp. 273–280.
- [13] Yao, Q., Dong, J., and Ferreira, P. M., 2008, "A Novel Parallel-Kinematics Mechanisms for Integrated, Multi-Axis Nanopositioning. Part 1. Kinematics and Design for Fabrication," *Precis. Eng.*, **32**(1), pp. 7–19.
- [14] Koseki, Y., Tanikawa, T., Koyachi, N., and Tatsuo, A., 2000, "Kinematic Analysis of Translational 3-DOF Micro Parallel Mechanism Using Matrix Method," Proceedings of the IEEE/RSJ International Conference on Intelligent Robots and Systems, Takamatsu, Japan, Oct. 31–Nov. 5, pp. 786–792.
- [15] Parikian, T. F., 1995, "Kinematic Analysis and Design of Parallel Robots," Technical Report No. 95-02, Swiss Federal Institute of Technology, Department of Microengineering.
- [16] Arakelian, V., 2018, *Dynamic Decoupling of Robot Manipulators*, Springer, New York.
- [17] Sarkar, N., Geisberger, A., and Ellis, M. D., 2004, "Fully Released MEMS XYZ Flexure Stage With Integrated Capacitive Feedback," US 6806991.
- [18] Liu, X., Kim, K., and Sun, Y., 2007, "A MEMS Stage for 3-Axis Nanopositioning," *J. Micromech. Microeng.*, **17**, pp. 1796–1802.
- [19] "Error Sources: Probe/Target Angle", Lion Precision Technical Brief, LT02-0012, March, 2004.